Fully spin-polarized hourglass charge-three Weyl points and sextuple-helicoid surface arcs in $P6_322$-type BaNiIO$_6$

Jianhua Wang,[1,2] Hongkuan Yuan,[1] Wenhong Wang,[2] Guangqian Ding,[3] Xiao-Ping Li ☉,[4,*] and Xiaotian Wang ☉[1,5,†]

[1]*School of Physical Science and Technology, Southwest University, Chongqing 400715, China*
[2]*School of Material Science and Engineering, Tiangong University, Tianjin 300387, China*
[3]*School of Science, Chongqing University of Posts and Telecommunications, Chongqing 400065, China*
[4]*School of Physical Science and Technology, Inner Mongolia University, Hohhot 010021, China*
[5]*Institute for Superconducting and Electronic Materials (ISEM), University of Wollongong, Wollongong, New South Wales 2500, Australia*

Magnetic topological materials exhibiting unique topological quantum physics due to the combination of spintronics and topology have aroused the interest of researchers. We propose $P6_322$-type BaNiIO$_6$—a dynamically stable material with two fully spin-polarized hourglass charge-three (C-3) Weyl points (WPs) and six fully spin-polarized charge-one (C-1) WPs around the Fermi level—with the help of first-principles calculations and symmetry analysis. C-3 WPs have been theoretically proposed for more than a decade. However, they have only been reported in nonmagnetic phonon systems rather than in magnetic electronic systems. $P6_322$-type BaNiIO$_6$ shows 100% spin polarization and belongs to the group of half-metals due to the metallic states and the semiconducting states for the bands in spin-up and spin-down directions, respectively. The half-metallic state and the spin-polarized C-3 and C-1 WPs are robust to uniform strains (from -5 to 5%) and on-site Hubbard-Coulomb interactions (from 0 to 6 eV). Furthermore, unique surface arcs connected the projections of two spin-polarized C-3 WPs and six spin-polarized C-1 WPs, leading to fully spin-polarized sextuple-helicoid surface arcs on the (001) surface of $P6_322$-type BaNiIO$_6$. Undoubtedly, $P6_322$-type BaNiIO$_6$, with fully spin-polarized C-3 and C-1 WPs and fully spin-polarized sextuple-helicoid surface arcs, is a promising candidate for applications in spintronic and topological physics.

I. INTRODUCTION

Current research has expanded from the conventional Weyl point (WP) [1–3] to multi-WPs [4–7] owing to advancement in the study of Weyl fermions in topological semimetals [8–12]. The conventional WP, i.e., the charge-one (C-1) WP [13–20], enjoys relativistic linear dispersion along any direction in momentum space; it can appear in three-dimensional (3D) crystals without any space group symmetry (except translation symmetry). Unlike conventional WPs with a chiral charge $|\mathcal{C}| = 1$, multi-WPs with higher $|\mathcal{C}|$ have also been proposed in theory. The WP with $|\mathcal{C}| = n$ ($n = 1, 2, 3, 4$) is also termed the charge-n (C-n) WP [21–34]. C-2 WPs with quadratic in-plane (along $k_{x,y}$) dispersion and C-3 WPs with cubic in-plane dispersion were theoretically proposed by Fang *et al.* [5] in 2012. C-2 WPs and C-3 WPs are protected by a fourfold or sixfold rotation symmetry and a sixfold rotation symmetry, respectively. Some solid-state materials have also been reported to be candidates with C-2 WPs in their electronic structures. For example, Fang *et al.* [5] proposed that the 3D ferromagnetic compound HgCr$_2$Se$_4$ is a fourfold rotation symmetry-protected multi-WP metal with two C-2 WPs along the Γ-Z path. Moreover, Huang *et al.* [6] proposed

that the stoichiometric compound strontium silicide, SrSi$_2$, is a multi-WP semimetal with C-2 WPs after including the spin-orbit coupling (SOC). Furthermore, C-4 WPs can be formed when cubic symmetry is combined with threefold screw rotational symmetry. Several independent groups [24,30–32] have reported C-4 WPs with $|\mathcal{C}| = 4$ in both spinless and spinful systems. C-4 WPs have a cubic dispersion along [111] and quadratic dispersions in all other directions. Some materials, such as LaIrSi-type materials [31], have already been reported to have C-4 WPs in both electronic systems and phonon spectra.

C-3 WPs with $|\mathcal{C}| = 3$ feature a linear dispersion along one direction and a cubic energy splitting in the plane normal to the direction. Wang *et al.* [33] and Liu *et al.* [34] recently reported C-3 WPs in phonon spectra of some real materials. Note that phonons [35–45], one kind of bosons, are good nonmagnetic platforms for obtaining spinless multi-WPs. Previous research on the material candidates with C-3 WPs has largely focused on nonmagnetic phononic systems; however, material candidates with C-3 WPs in magnetic electronic systems have not been studied. For a long time, researchers have attempted to discover novel topological states and new topological features and application possibilities in magnetic systems [46–74]. Particularly, it is most attractive when the magnetic system is a half-metal with 100% spin polarization, i.e., the bands around the Fermi level belong to one spin direction. The topological states in one spin direction for the

*Corresponding author: xpli@imu.edu.cn
†Corresponding author: xiaotianwang@swu.edu.cn

topological half-metals [75] are fully spin polarized, which has great potential in spintronics applications.

This work, with the help of first-principles calculations, reveals $P6_322$-type BaNiIO$_6$ as a fully spin-polarized hourglass C-3 WP half-metal. $P6_322$-type BaNiIO$_6$ has the following *exotic features*. (i) Fully spin-polarized WPs, i.e., two hourglass C-3 WPs and six conventional C-1 WPs, appear in the 3D Brillouin zone (BZ). The appearance of hourglass C-3 WPs in a magnetic system is notable. (ii) The two hourglass C-3 WPs and the six C-1 WPs constitute a fully spin-polarized Weyl complex for which the net topological charge vanishes. The appearance of a fully spin-polarized Weyl complex formed by C-3 and C-1 WPs is notable. (iii) The two hourglass C-3 WPs and six conventional C-1 WPs are robust to uniform strains (from −5 to 5%) and on-site Hubbard-Coulomb interactions (from 0 to 6 eV for the Ni-d orbitals). (iv) Fully spin-polarized sextuple-helicoid surface arcs on the (001) surface are formed by connecting the projections of the two hourglass C-3 WPs and six conventional C-1 WPs. The appearance of fully spin-polarized sextuple-helicoid surface arcs in a magnetic system is notable. Our work shows a magnetic topological state with a fully spin-polarized Weyl complex (formed by two hourglass C-3 WPs and six C-1 WPs) and fully spin-polarized sextuple-helicoid surface arcs in a ferromagnet, which may have promising applications in spintronics.

II. COMPUTATIONAL METHODS

The first-principles calculations were performed within the framework of density functional theory (DFT) [76]; the projector augmented wave method was applied as implemented in the Vienna *ab initio* simulation package (VASP) [77]. The exchange-correlation potential of the Perdew-Burke-Ernzerhof (PBE) [78] functional was used with the generalized gradient approximation (GGA). The energy cutoff of 500 eV was set for the plane wave basis, and a k mesh of a $7 \times 7 \times 3$ Monkhorst-Pack grid was sampled for the first Brillouin zone. The calculation of the structural relaxation and self-consistent iteration was fully converged until the total residual force per atom was less than −0.01 eV/Å and the total energy variation per atom was smaller than 1×10^{-6} eV. To study the surface states for the (001) surfaces, we constructed an *ab initio* tight-binding model based on the Wannier functions [79]. The surface spectra were investigated by using this model and by the iterative Green's function method [80,81].

III. STABILITY AND MAGNETISM

The crystal structure for $P6_322$-type BaNiIO$_6$ is shown in Fig. 1(a). The Ba, Ni, I, and O atoms are located at the 2a, 2d, 2c, and 12i Wyckoff sites in the structure, respectively. The theoretically obtained lattice constants for $P6_322$-type BaNiIO$_6$ are $a = b = 5.18$ Å and $c = 11.7$ Å.

The phonon dispersions of $P6_322$-type BaNiIO$_6$ along the Γ-M-K-Γ-A-L-H-$A|L$-$M|H$-K high-symmetry paths [see Fig. 1(b)] were added using the density functional perturbation theory [82]. A supercell of $2 \times 2 \times 2$ was adopted to calculate force constants. Figure 1(c) shows that $P6_322$-type
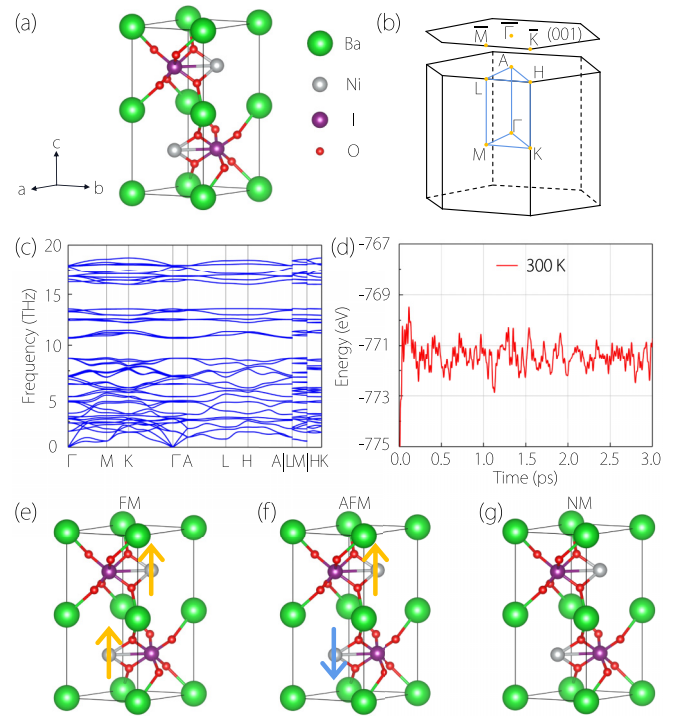
FIG. 1. (a) Crystal structure for $P6_322$-type BaNiIO$_6$. (b) 3D bulk and 2D surface BZs. (c) Phonon dispersion for $P6_322$-type BaNiIO$_6$ along the Γ-M-K-Γ-A-L-H-$A|L$-$M|H$-K paths. (d) Total energy fluctuation of a $2 \times 2 \times 2$ BaNiIO$_6$ supercell during *ab initio* molecular dynamics (AIMD) simulations at 300 K. (e)–(g) Three magnetic configurations: ferromagnetic (FM), antiferromagnetic (AFM), and nonmagnetic configurations (NM) for $P6_322$-type BaNiIO$_6$.

BaNiIO$_6$ is a dynamically stable material due to the lack of imaginary modes. The elastic constants were obtained to evaluate the mechanical stability of $P6_322$-type BaNiIO$_6$. The following are six independent elastic constants for the hexagonal: C_{11}, C_{12}, C_{13}, C_{33}, C_{44}, and C_{66}, which were estimated by the stress-strain method. The results of the six elastic constants are listed in Table I. The following are the elastic stability criteria [83]:

$$C_{11} > |C_{12}|, \quad 2C_{13}^2 < C_{33}(C_{11} + C_{12}), \quad C_{44} > 0. \quad (1)$$

The elastic constants of $P6_322$-type BaNiIO$_6$ satisfy all the criteria mentioned above, which implies mechanical stability.

$P6_322$-type BaNiIO$_6$ has not been synthesized. The structural stability of $P6_322$-type BaNiIO$_6$ can be evaluated from the formation energy defined as follows:

$$E_{\text{form}}(\text{BaNiIO}_6) = E(\text{BaNiIO}_6) - [2E(\text{Ba})$$
$$+ 2E(\text{Ni}) + 2E(\text{I}) + 12E(\text{O})], \quad (2)$$

TABLE I. Obtained elastic constants (in GPa) for $P6_322$-type BaNiIO$_6$.

C_{11}	C_{12}	C_{13}	C_{33}	C_{44}	C_{66}
157.403	97.778	47.68	119.938	31.466	31.312

TABLE II. Total energy E_{total} (in meV) obtained for the FM, AFM, and NM magnetic configurations shown in Figs. 1(e)–1(g). The values were calculated using the GGA + SOC with different U values (from 0 to 6 eV for Ni-d orbitals). The FM$_{[110]}$ configuration is the ground state; it was set to 0 eV for reference.

| | E_{total} (meV) | | | | | | | | | | | | | | |
| | FM | | | | | | | AFM | | | | | | | NM |
U (eV)	[100]	[010]	[001]	[110]	[101]	[011]	[111]	[100]	[010]	[001]	[110]	[101]	[011]	[111]	
$U=0$	0.39122	0.75587	0.27836	0	0.09949	0.14521	0.09844	5.27114	5.22008	5.50192	5.28712	5.59672	5.42824	5.20106	144.41811
$U=1$	0.44311	0.76744	0.30692	0	0.12535	0.15886	0.10754	5.82529	5.76932	6.07828	5.76991	6.25892	5.92336	5.87211	189.16727
$U=2$	0.47782	0.90635	0.32306	0	0.14843	0.16713	0.11299	6.26544	6.24181	6.52736	6.24179	6.83079	6.37326	6.32634	226.74503
$U=3$	0.50301	0.6418	0.32364	0	0.16979	0.16566	0.11148	6.76224	6.72746	6.95074	6.72805	7.3888	6.83471	6.79963	256.32577
$U=4$	0.40633	0.58872	0.3331	0	0.23329	0.17959	0.12409	7.18967	7.15118	7.36887	7.15234	7.87444	7.25675	7.01499	277.46239
$U=5$	0.46063	0.46704	0.32872	0	0.30901	0.1595	0.10439	7.54369	7.50557	7.71996	7.50602	8.26377	7.60984	7.57735	289.81059
$U=6$	0.50914	0.44159	0.3239	0	0.2558	0.16681	0.112	7.81952	7.90466	7.99389	7.78295	8.55072	7.88603	7.85356	293.2822

where $E_{form}(BaNiIO_6)$ is the energy per atom of the $BaNiIO_6$ material, while $E(Ba)$, $E(Ni)$, $E(I)$, and $E(O)$ are its counterparts for the most stable elemental phases. The formation energy is calculated to be -1.1314 eV/atom, reflecting the stability of $P6_3 22$-type $BaNiIO_6$.

The thermodynamic stability of a $2 \times 2 \times 2$ superlattice of $BaNiIO_6$ was tested via *ab initio* molecular dynamics (AIMD) [84] at 300 K in the framework of the Nosé-Hoover thermostat ensemble. The results are shown in Fig. 1(d). During the simulation, the total energy remained approximately invariant with respect to time, indicating the room-temperature stability of the $BaNiIO_6$.

The magnetic ground state of $P6_3 22$-type $BaNiIO_6$ should be determined before analyzing the electronic structure. The element Ni in $BaNiIO_6$ carries a nonzero magnetic moment; these moments spontaneously order in the ground state. Three magnetic configurations—ferromagnetic (FM), antiferromagnetic (AFM), and nonmagnetic configurations (NM)—were considered to examine the magnetic ground state of $BaNiIO_6$ [see Figs. 1(e)–1(g)]. We considered seven possible orientations of the magnetic moments for each of the AFM and FM states, namely, the [100], [010], [001], [110], [101], [011], and [111] directions. The results are shown in Table II. Note that the values in Table II were calculated using the GGA+SOC with the Hubbard-Coulomb interaction U varying from 0 to 6 eV for Ni-d orbitals. Table II shows that the lowest energy appears for the FM$_{[110]}$ configuration. Table III shows measured total and atomic magnetic moments for $P6_3 22$-type $BaNiIO_6$. Different magnetic configurations in the $2 \times 2 \times 1$ and $1 \times 1 \times 2$ supercells are also presented in Figs. S1 and S2 of the Supplemental Material (SM) [85]. We found that the optimized FM state is the most energetically stable in all magnetic configurations and has lower energy than the AFM and NM states. In the following section, $BaNiIO_6$ with

the FM$_{[110]}$ configuration was used to study the half-metallic properties and band structures.

IV. FULLY SPIN-POLARIZED HOURGLASS C-3 AND C-1 WPs AND RELATED FULLY SPIN-POLARIZED WEYL COMPLEX

Figures 2(a) and 2(b) show the spin-up and spin-down band structures as well as the density of states for the $P6_3 22$-type $BaNiIO_6$, respectively. In the spin-down channel, a noticeable energy gap with a large value (~ 1.28 eV) can be observed; that is, the bands in the spin-down channel show semiconducting properties. However, the bands in the spin-up channel
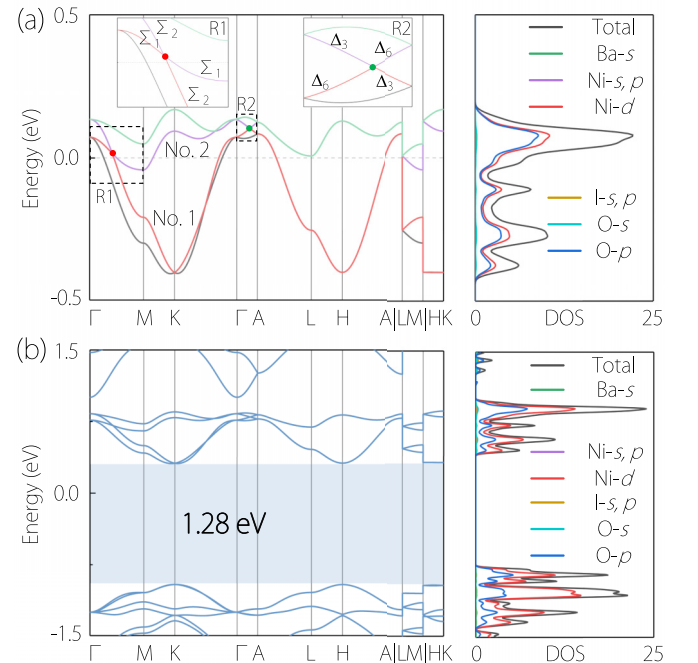
FIG. 2. (a) and (b) Spin-up and spin-down band structures as well as the density of states (DOS) for $P6_3 22$-type $BaNiIO_6$, respectively. In (a) we show the irreducible representation of the two bands (bands 1 and 2) in regions R1 and R2.

TABLE III. Total and atomic magnetic moments (μ_B) in the $BaNiIO_6$ primitive cell.

Total	Ba	Ni	I	O
1.887	0.007	0.741	0.003	0.032
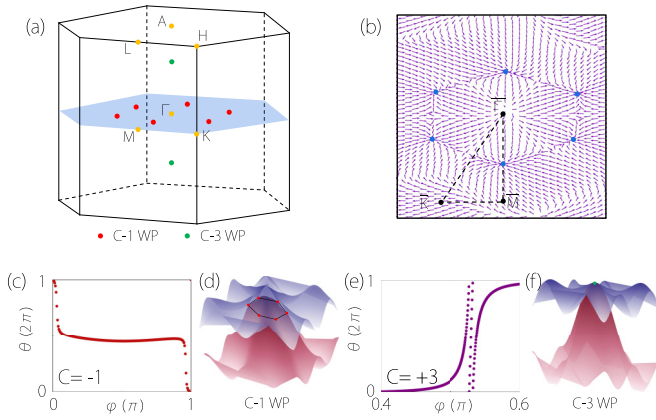
FIG. 3. (a) 3D BZ and the positions of the two hourglass C-3 WPs (green balls) and the six C-3 WPs (red balls). (b) The distribution of the Berry curvature in the k_x-k_y plane. (c) and (e) Evolutions of the average position of the Wannier center for the C-1 WP with $\mathcal{C} = -1$ and the C-3 WP with $\mathcal{C} = +3$, respectively. (d) and (f) 3D plots of the bands around the C-1 WPs and C-3 WP, respectively.

show metallic properties, meaning that the bands and the Fermi level are overlapped.

After that, we investigated the topological states around the Fermi level in the spin-up channel. Figure 2(a) shows that two obvious band crossing points are formed by the crossings of bands 1 and 2 around the Fermi level. The band crossing point on the Γ-M path hosts a $\mathcal{C}$ of -1 and enjoys linear band dispersion along any direction in momentum space [see Figs. 3(c) and 3(d)]. Hence the band crossing point on the Γ-M path belongs to C-1 WP. After careful scanning, we found six C-1 WPs at the $k_z = 0$ plane. The momentum positions for these C-1 WPs are shown in Table IV and Fig. 3(a).

Furthermore, we studied the protection of the band crossing points. We note that the points are located at the C'_{21} invariant line (Γ-M path); each band can be further labeled by the eigenvalues of C'_{21} symmetry. We found [see Fig. 2(a)] that the conduction and valence bands have opposite eigenvalues ± 1. Therefore the stable existence of the Weyl point is protected. The matrix representations of symmetry operations can be expressed as $C'_{21} = \sigma_z$ and the antiunitary operation $C''_{21}\mathcal{T} = \sigma_0$. The effective Hamiltonian around the Γ-M path is given as follows:

$$\mathcal{H}_{C\text{-}1}(\boldsymbol{k}) = c_1 k_x \sigma_0 + c_2 k_x \sigma_z + c_3 k_z \sigma_x + c_4 k_y \sigma_y, \quad (3)$$

TABLE IV. Band index, locations, momentum positions, and Chern number of the spin-polarized WPs around the Fermi level.

Bands	Location	Momentum position	Chern number
1 and 2	Γ-M path	$(0.21, 0, 0)$	-1
1 and 2	Γ-M' path	$(-0.21, 0, 0)$	-1
1 and 2	Γ-M' path	$(0, 0.21, 0)$	-1
1 and 2	Γ-M' path	$(0, -0.21, 0)$	-1
1 and 2	Γ-M' path	$(0.21, -0.21, 0)$	-1
1 and 2	Γ-M' path	$(-0.21, 0.21, 0)$	-1
1 and 2	Γ-A path	$(0, 0, 0.317)$	$+3$
1 and 2	Γ-A' path	$(0, 0, -0.317)$	$+3$

where σ_i ($i = x, y, z$) are the Pauli matrices and σ_0 denotes the 2×2 identity matrix; c_i's are real parameters. This Hamiltonian demonstrates that the band crossing at the Γ-M path is a linear C-1 WP.

Besides the C-1 WP on the Γ-M path, a band crossing point can be found on the Γ-A path. Interestingly, the band crossing point is the neck crossing point of the hourglasslike dispersions. We note that the hourglass fermions [86], where four bands are entangled into groups with hourglass-shaped dispersions, have recently stimulated widespread interest [87–91]. $\mathcal{C}$ for the band crossing point on the Γ-A path equals $+3$ [see Fig. 3(e)]; this point shows a linear dispersion along the Γ-A path and a cubic dispersion in the plane perpendicular to the Γ-A path [see Fig. 3(f)]. This crossing point is an hourglass C-3 WP. Another C-3 WP with $\mathcal{C} = +3$ appears on the Γ-A' path because $P6_322$-type BaNiIO$_6$ has $\mathcal{T}$ symmetry. The momentum positions for these two C-3 WPs are shown in Table IV and Fig. 3(a).

We note that the little cogroup on the Γ-A path is C_6. Furthermore, the crossing bands are found to form two distinct one-dimensional irreducible representations Δ_3 and Δ_6 of a cyclic group [see Fig. 2(a)]. The corresponding eigenvalues of $\widetilde{C}_{6z} = \{C_{6z}|00\frac{1}{2}\}$ are $e^{\frac{i\pi}{3}}$ and $e^{-\frac{2i\pi}{3}}$, respectively. Therefore these bands can be hybridized along this line, and their crossing points are protected. We constructed a $\boldsymbol{k} \cdot \boldsymbol{p}$ effective model based on symmetry to characterize the C-3 WP. The basis was chosen as eigenstates of $\widetilde{C}_{6z}$ with $|e^{\frac{i\pi}{3}}\rangle \oplus |e^{-\frac{2i\pi}{3}}\rangle$; the matrix representations of the generators can be expressed as $\widetilde{C}_{6z} = e^{\frac{i\pi}{3}}\sigma_z$, $C''_{23}\mathcal{T} = \sigma_0$. Ultimately, the effective model for the Γ-A path expanded up to the leading order reads

$$\mathcal{H}_{C\text{-}3}(\boldsymbol{k}) = \mathcal{H}_0(\boldsymbol{k}) + [c_1(k_+^3 + k_-^3)\sigma_+ + \text{H.c.}], \quad (4)$$

with

$$\mathcal{H}_0(\boldsymbol{k}) = \sum_{i=0,x,y,z} \sigma_i \big[c_{i,1} k_z + c_{i,2} k_z^2$$
$$+ c_{i,3} k_z^3 + (c_{i,4} + c_{i,5} k_z)\boldsymbol{k}^2 \big], \quad (5)$$

where $c_{i,j}$ are real parameters, $\boldsymbol{k}^2 = k_x^2 + k_y^2 + k_z^2$, $k_\pm = k_x \pm ik_y$, and $\sigma_\pm = \sigma_x \pm i\sigma_x$. Equation (4) shows that band crossing has a linear dispersion along the k_z direction and a cubic dispersion in the k_x-k_y plane, indicating the presence of a C-3 WP.

Figure 3(b) shows the distribution of the Berry curvature contributed by bands 1 and 2 in the k_x-k_y plane. Due to their chirality, the Berry curvature near hourglass C-3 WPs and C-1 WPs shows divergent and convergent field morphology. Moreover, bands 1 and 2 form two C-3 WPs with $\mathcal{C} = +3$ and six C-1 WPs with $\mathcal{C} = -1$, yielding a system with a zero net topological charge that rigorously obeys the Nielsen-Ninomiya no-go theory [92,93]. The two C-3 WPs with $\mathcal{C} = +3$ and six C-1 WPs are fully spin polarized. These WPs form a unique, fully spin-polarized Weyl complex, where the net $\mathcal{C}$ disappears.

Finally, we note the following points: (1) The hourglass C-3 WPs and the C-1 WPs formed by bands 1 and 2 are quite clean. No other extraneous band crossing points (formed by bands 1 and 2) around the Fermi level are found. (2) We choose the s orbital of the Ba atoms, the s, p, and d orbitals of the Ni atoms, the s and p orbitals of the I atoms, and the s and p
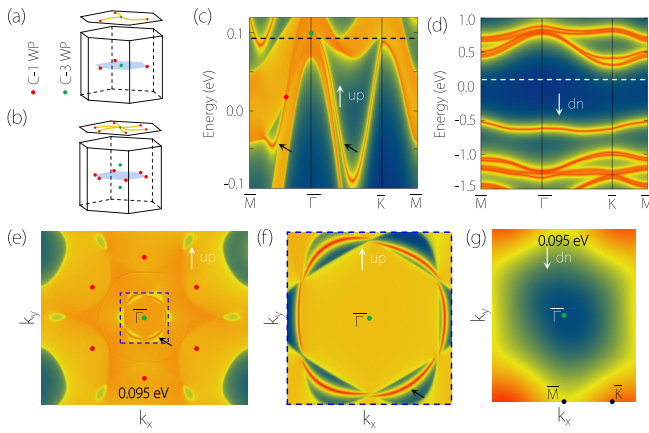
FIG. 4. (a) and (b) Schematic diagrams of the triple-helicoid surface arcs and sextuple-helicoid surface arcs, respectively. (c) and (d) Projected spectrum on the (001) surface of $P6_3 22$-type BaNiIO$_6$ in the spin-up and spin-down channels, respectively. (e) and (g) Constant-energy slices at 0.095 eV for the spin-up and spin-down channels, respectively. (f) Enlarged region of the dashed box in (e). Surface modes in (c), (e), and (f) are marked by black arrows. These surface modes appear in a single-spin channel with full spin polarization. Here, dn, down.

orbitals of the O atoms as projections for the Wannierization. The band structures obtained by Wannierization are in good agreement with those obtained by DFT (see Fig. S3 of the SM [85]). (3) The hourglass C-3 WPs and the C-1 WPs are close to the Fermi level; the energy values for the hourglass C-3 WPs and the C-1 WPs are about 0.10 and 0.01 eV, respectively. (4) We can induce an electron doping effect into $P6_3 22$-type BaNiIO$_6$ to adjust the location of the Fermi level. As shown in Fig. S4 of the SM [85], with an electron doping concentration of 0.06 carriers per atom, the Fermi level of $P6_3 22$-type BaNiIO$_6$ will move towards a higher energy level, and the C-3 WPs are exactly at the Fermi level. (5) Since the band dispersion would affect the shape of the Fermi surface and then determine the majority of material properties, the cubic nodal point should manifest signatures that are distinct from those of the linear nodal point. Since we found no report of a cubic Weyl point appearing in an experiment, we use the cubic and linear Dirac points as examples to compare the effects associated with their relative dispersions. A linear Dirac point may exhibit negative magnetoresistance [94,95], a special magnetic oscillation frequency driven by surface Fermi arcs [96], and an artificial gravity field through strain modulation [97]. A cubic Dirac point may display unusual quantum interference contributions to magnetotransport [98], stronger screening of interactions, and the potential presence of continuous quantum phase transitions driven by interactions [99].

V. FULLY SPIN-POLARIZED SEXTUPLE-HELICOID SURFACE ARCS

Topological Weyl semimetals show a Fermi arc state on the boundary of the system. The Fermi arc state around the projected point of the WP has chirality-dependent features [24]. Three Fermi arcs are found in the C-3 WP semimetal

[as shown in Fig. 4(a)] because the hourglass C-3 WP hosts a $|\mathcal{C}| = 3$.

Figure 4(b) shows that the two bulk C-3 WPs for $P6_3 22$-type BaNiIO$_6$ are projected to the same position, namely, the $\overline{\Gamma}$ surface point in the (001) surface BZ. Therefore six surface arcs connected to the $\overline{\Gamma}$ surface point must exist, leading to a sextuple-helicoid surface arc mode [as schematically shown in Fig. 4(b)] due to the $\mathcal{C} = +6$ ($+3 \times 2$).

Figure 4(e) depicts the slice at constant energy $E = 0.095$ eV [see the dashed line in Fig. 4(c)] on the (001) surface for the spin-up channel of $P6_3 22$-type BaNiIO$_6$. We enlarged the dashed box of Fig. 4(e), as shown in Fig. 4(f). The results of our calculation show the expected sextuple-helicoid surface mode. The fully spin-polarized helicoid surface mode is expected for the $P6_3 22$-type BaNiIO$_6$ studied in this paper because the bulk has fully spin-polarized C-3 and C-1 WPs. The sextuple-helicoid surface mode only appears in the spin-up channel of $P6_3 22$-type BaNiIO$_6$, implying full spin polarization. No surface modes are found around the Fermi level in the spin-down channel of $P6_3 22$-type BaNiIO$_6$ [see Figs. 4(d) and 4(g)].

VI. ROBUSTNESS OF SPIN-POLARIZED C-3 AND C-1 WPs UNDER ON-SITE HUBBARD-COULOMB INTERACTIONS U

The spin-polarized band structures plotted in Fig. 2 did not consider the on-site Hubbard-Coulomb interactions U. Therefore one may wonder about the robustness of our result in the presence of variation in U. Hence we checked the results for U values up to 6 eV for Ni-d orbitals to examine this question. The orbital-resolved band structures for BaNiIO$_6$ contributed by Ni-d orbitals in the spin-up and spin-down channels are shown in Fig. S5 of the SM [85]. Changing the U parameter for Ni-d orbitals will affect the positions of the WPs in the spin-up channel and the semiconducting gap in the spin-down channel [see Figs. 5(a) and 5(b)].

The essential band features, including the half-metallic behavior and the hourglass C-3 and C-1 WPs, are maintained in the presence of variations in U up to 6 eV. Figures 5(a) and 5(b) show the conduction band minimum (CBM) and the valence band maximum (VBM) in the spin-down channel and the positions of hourglass C-3 and C-1 WPs around the Fermi level in the spin-up channel, respectively. For clarity, the spin-polarized band structures of $P6_3 22$-type BaNiIO$_6$ with $U = 2$, 4, and 6 eV for Ni-d orbitals are given in Figs. 5(c), 5(d), and 5(e), respectively. The $P6_3 22$-type BaNiIO$_6$ is still a half-metal with the coexistence of the hourglass C-3 and C-1 WPs with different U values. The low-energy bands around the Fermi level in the spin-up channel in Figs. 5(c), 5(d), and 5(e) are very similar to the result in Fig. 2.

VII. ROBUSTNESS OF SPIN-POLARIZED C-3 AND C-1 WPs UNDER DIFFERENT UNIFORM STRAINS

This section discusses the study of the robustness of spin-polarized C-3 and C-1 WPs under different uniform strains. We carried out the uniform strains by changing the lattice constants a, b, and c simultaneously. Table V clarifies the relationship between uniform strains and the lattice constants.

TABLE V. The relationship between uniform strains and the lattice constants.

Lattice constants	Uniform strain										
	−5%	−4%	−3%	−2%	−1%	0%	1%	2%	3%	4%	5%
$a = b$ (Å)	4.921	4.9728	5.0246	5.0764	5.1282	5.18	5.2318	5.2836	5.3354	5.3872	5.439
c (Å)	11.115	11.232	11.349	11.466	11.583	11.7	11.817	11.934	12.051	12.168	12.285

Uniform strains from −5 to 5% were considered. The key band features, such as the CBM and VBM values in the spin-down channel [see Fig. 6(a)] and the positions of the hourglass C-3 and C-1 WPs in the spin-up channel [see Fig. 6(b)], display robustness against the variation in uniform strain. For instance, Figs. 6(c) and 6(d) show spin-polarized band structures of BaNiO$_6$ with −5 and 5% uniform strain. The strained systems are still half-metals, and the low-energy bands around the Fermi level in the spin-up channel are very similar to the result shown in Fig. 2.

VIII. EFFECT OF SOC ON THE BAND CROSSING POINTS

This section presents the study on the effect of SOC on the hourglass C-3 and C-1 WPs around the Fermi level. The band structure calculated with GGA+SOC is shown in Fig. 7(a). Furthermore, the band structure calculated with GGA+SOC + U (6 eV for Ni-d orbitals) is shown in Fig. 7(b). We primarily focus on the crossing points in regions R3, R4, R5, and R6. The enlarged bands in regions R3, R4, R5, and R6 are shown in Figs. 7(c), 7(d), 7(e), and 7(f), respectively.

We note that the spin has SU(2) symmetry in the absence of SOC, and the spin orientation does not affect the orbital part of the wave function. Each spin channel can be regarded as a spinless system; the C-1 and C-3 Weyl points can be stabilized by C'_{21} and $\widetilde{C}_{6z}$ symmetries, respectively. However, these two

symmetries would break and a band gap is expected when the SOC effect is present and the magnetization direction is [110].

Fortunately, our calculations suggest that the SOC-induced gap at the hourglass C-3 and C-1 WPs is quite small (<2 meV) [Figs. 7(c)–7(f)]. Note that the value of the SOC-induced gap is below the resolution of angle-resolved photoemission spectroscopy (ARPES) and significantly lower than the energy scale of room temperature (26 meV). Specifically, such small SOC-induced gaps at the hourglass C-3 and C-1 WPs would hardly be detected in ARPES due to the ignorable thermal broadening effect.

IX. FERROMAGNETISM AND TOPOLOGICAL SIGNATURES OF BaNiO$_6$ UNDER THE SCAN META-GGA FUNCTIONAL

As mentioned by Sun *et al.* [100], the strongly constrained and appropriately normed (SCAN) meta-GGA functional [101] matches or improves on the accuracy of a computationally expensive hybrid functional, at almost-GGA cost. In this paper, we therefore utilized the SCAN meta-GGA functional to check the magnetic ground state and the topological signatures of $P6_322$-type BaNiO$_6$.

The results of the total energy E$_{total}$ (in meV) obtained for FM, AFM, and NM magnetic configurations are shown in Table S1 of the SM [85]. We considered seven possible orientations of the magnetic moments for the AFM and FM states, namely, the [100], [010], [001], [110], [101], [011], and
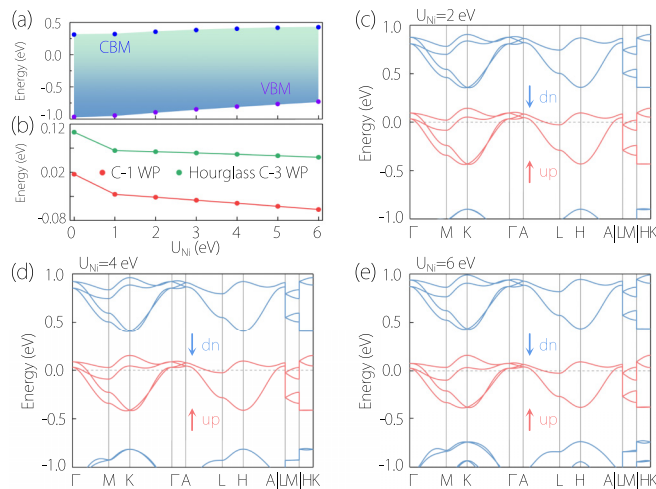
FIG. 5. (a) and (b) CBM and VBM (in the spin-down channel) and the positions of the hourglass C-3 and C-1 WPs (in the spin-up channel) as functions of U values from 0 to 6 eV for Ni-d orbitals. (c), (d), and (e) Spin-polarized band structures of $P6_322$-type BaNiO$_6$ with $U = 2$, 4, and 6 eV for Ni-d orbitals, respectively.
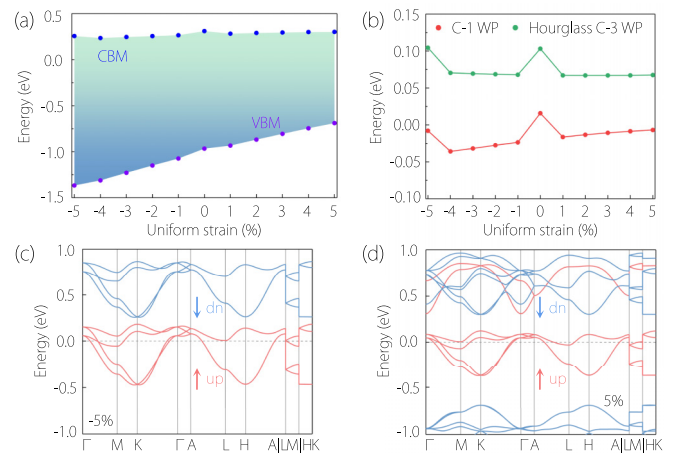
FIG. 6. (a) and (b) CBM and VBM (in the spin-down channel) and the positions of the hourglass C-3 and C-1 WPs (in the spin-up channel) as functions of −5 to 5% uniform strains. (c) and (d) Spin-polarized band structures of $P6_322$-type BaNiO$_6$ with −5 and 5% uniform strains, respectively.
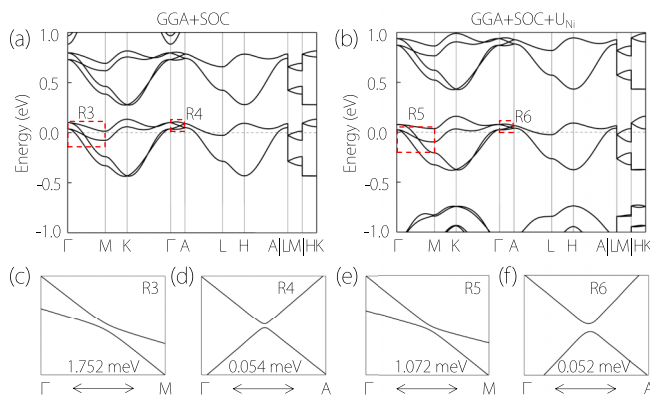
FIG. 7. (a) and (b) The band structures of $P6_322$-type BaNiIO$_6$ calculated using the GGA+ SOC and GGA + SOC + U (6 eV for Ni-d orbitals), respectively. (c), (d), (e), and (f) The enlarged band structures of regions R3, R4, R5, and R6, respectively.

[111] directions. One can see that the FM$_{[011]}$ configuration is the determined magnetic ground state of BaNiIO$_6$ under the SCAN meta-GGA functional.

Comparing the magnetic ground states obtained by the GGA $+ U$ and SCAN meta-GGA functionals reveals that according to both functionals, FM is the most stable magnetic state. Nonetheless, the preferred magnetization orientations of the magnetic moments for the FM state determined by the GGA $+ U$ and SCAN meta-GGA are different, i.e., FM$_{[110]}$ for GGA $+ U$ and FM$_{[011]}$ for SCAN meta-GGA. Under FM$_{[011]}$, we calculated the band structure using the SCAN meta-GGA functional. The band structures calculated using the SCAN meta-GGA are similar to those calculated using the GGA. One finds that all the C-1 and C-3 WPs near the Fermi level are retained in $P6_322$-type BaNiIO$_6$ (see Fig. S6 of the SM [85]). The momentum positions and Chern numbers for these C-1 and C-3 WPs are shown in Table S2 (see SM [85]).

Furthermore, we calculated the band structure of $P6_322$-type BaNiIO$_6$ with SCAN meta-GGA+SOC (the magnetization direction was [011]). Figure S7 (see

SM [85]) demonstrates that the SOC-induced gaps at the hourglass C-3 and C-1 WPs are still quite small (<6 meV) and significantly below the energy scale at room temperature (26 meV).

Consequently, one can conclude that the ferromagnetism and topological signatures of BaNiIO$_6$ have not changed despite the fact that the functional has been changed from the GGA to the SCAN meta-GGA.

X. SUMMARY

We predict that $P6_322$-type BaNiIO$_6$ is thermodynamically, mechanically, and dynamically stable in a hexagonal crystal structure with the $P6_322$ space group. The ground state of $P6_322$-type BaNiIO$_6$ is ferromagnetic. It hosts a metallic state in the spin-up channel and a semiconducting state in the spin-down channel, reflecting that it is a ferromagnetic half-metal. The bands (bands 1 and 2) around the Fermi level in the spin-up channel form two hourglass C-3 WPs (with $\mathcal{C} = +3$) and six C-1 WPs ($\mathcal{C} = -1$) in the 3D BZ, further constructing a Weyl complex with zero net $\mathcal{C}$. They are fully spin polarized because the hourglass C-3 WPs, the C-1 WPs, and the Weyl complex only appear in a single-spin channel. The fully spin-polarized Weyl complex leads to sextuple-helicoid surface arcs on the (001) surface that are also fully spin polarized, i.e., the surface modes around the Fermi level only appear in the spin-up channel. This report of fully spin-polarized hourglass C-3 WPs and fully spin-polarized sextuple-helicoid surface modes *in a half-metallic material* is notable. Such a ferromagnetic Weyl complex, formed by C-3 and C-1 WPs, and the related sextuple-helicoid surface arcs may have possible applications in spintronics.

[1] S. Murakami, New J. Phys. **9**, 356 (2007).

[2] X. Wan, A. M. Turner, A. Vishwanath, and S. Y. Savrasov, Phys. Rev. B **83**, 205101 (2011).

[3] S. M. Young, S. Zaheer, J. C. Y. Teo, C. L. Kane, E. J. Mele, and A. M. Rappe, Phys. Rev. Lett. **108**, 140405 (2012).

[4] G. Xu, H. Weng, Z. Wang, X. Dai, and Z. Fang, Phys. Rev. Lett. **107**, 186806 (2011).

[5] C. Fang, M. J. Gilbert, X. Dai, and B. A. Bernevig, Phys. Rev. Lett. **108**, 266802 (2012).

[6] S.-M. Huang, S.-Y. Xu, I. Belopolski, C.-C. Lee, G. Chang, T.-R. Chang, B. Wang, N. Alidoust, G. Bian, M. Neupane, D. Sanchez, H. Zheng, H.-T. Jeng, A. Bansil, T. Neupert, H. Lin, and M. Z. Hasan, Proc. Natl. Acad. Sci. USA **113**, 1180 (2016).

[7] S. S. Tsirkin, I. Souza, and D. Vanderbilt, Phys. Rev. B **96**, 045102 (2017).

[8] B. Yan and C. Felser, Annu. Rev. Condens. Matter Phys. **8**, 337 (2017).

[9] B. Q. Lv, H. M. Weng, B. B. Fu, X. P. Wang, H. Miao, J. Ma, P. Richard, X. C. Huang, L. X. Zhao, G. F. Chen, Z. Fang, X. Dai, T. Qian, and H. Ding, Phys. Rev. X **5**, 031013 (2015).

[10] M. M. Vazifeh and M. Franz, Phys. Rev. Lett. **111**, 027201 (2013).

[11] H.-X. Wang, Z.-K. Lin, B. Jiang, G.-Y. Guo, and J.-H. Jiang, Phys. Rev. Lett. **125**, 146401 (2020).

[12] J. Ruan, S.-K. Jian, D. Zhang, H. Yao, H. Zhang, S.-C. Zhang, and D. Xing, Phys. Rev. Lett. **116**, 226801 (2016).

[13] H. Weng, C. Fang, Z. Fang, B. A. Bernevig, and X. Dai, Phys. Rev. X **5**, 011029 (2015).

[14] L. X. Yang, Z. K. Liu, Y. Sun, H. Peng, H. F. Yang, T. Zhang, B. Zhou, Y. Zhang, Y. F. Guo, M. Rahn, D. Prabhakaran, Z.

Hussain, S. Mo, C. Felser, B. Yan, and Y. L. Chen, Nat. Phys. **11**, 728 (2015).

[15] A. A. Soluyanov, D. Gresch, Z. Wang, Q. Wu, M. Troyer, X. Dai, and B. A. Bernevig, Nature (London) **527**, 495 (2015).

[16] Y. Sun, S.-C. Wu, M. N. Ali, C. Felser, and B. Yan, Phys. Rev. B **92**, 161107(R) (2015).

[17] G. Autès, D. Gresch, M. Troyer, A. A. Soluyanov, and O. V. Yazyev, Phys. Rev. Lett. **117**, 066402 (2016).

[18] W. Shi, L. Muechler, K. Manna, Y. Zhang, K. Koepernik, R. Car, J. van den Brink, C. Felser, and Y. Sun, Phys. Rev. B **97**, 060406(R) (2018).

[19] Q. Xu, E. Liu, W. Shi, L. Muechler, J. Gayles, C. Felser, and Y. Sun, Phys. Rev. B **97**, 235416 (2018).

[20] G. Chang, S.-Y. Xu, D. S. Sanchez, S.-M. Huang, C.-C. Lee, T.-R. Chang, H. Zheng, G. Bian, I. Belopolski, N. Alidoust, H.-T. Jeng, A. Bansil, H. Lin, and M. Z. Hasan, Sci. Adv. **2**, e1600295 (2016).

[21] T. Zhang, Z. Song, A. Alexandradinata, H. Weng, C. Fang, L. Lu, and Z. Fang, Phys. Rev. Lett. **120**, 016401 (2018).

[22] H. Miao, T. T. Zhang, L. Wang, D. Meyers, A. H. Said, Y. L. Wang, Y. G. Shi, H. M. Weng, Z. Fang, and M. P. M. Dean, Phys. Rev. Lett. **121**, 035302 (2018).

[23] Z.-M. Yu, W. Wu, Y. X. Zhao, and S. A. Yang, Phys. Rev. B **100**, 041118(R) (2019).

[24] C. Cui, X.-P. Li, D.-S. Ma, Z.-M. Yu, and Y. Yao, Phys. Rev. B **104**, 075115 (2021).

[25] G. Ding, J. Wang, Z.-M. Yu, Z. Zhang, W. Wang, and X. Wang, Phys. Rev. Mater. **7**, 014202 (2023).

[26] X. Wang, F. Zhou, Z. Zhang, W. Wu, Z.-M. Yu, and S. A. Yang, Phys. Rev. B **106**, 195129 (2022).

[27] C. Chen, Z.-M. Yu, S. Li, Z. Chen, X.-L. Sheng, and S. A. Yang, Phys. Rev. B **99**, 075131 (2019).

[28] Z. Zhu, Y. Liu, Z.-M. Yu, S.-S. Wang, Y. X. Zhao, Y. Feng, X.-L. Sheng, and S. A. Yang, Phys. Rev. B **98**, 125104 (2018).

[29] Z.-M. Yu, Z. Zhang, G.-B. Liu, W. Wu, X.-P. Li, R.-W. Zhang, S. A. Yang, and Y. Yao, Sci. Bull. **67**, 375 (2022).

[30] Q.-B. Liu, Z. Wang, and H.-H. Fu, Phys. Rev. B **103**, L161303 (2021).

[31] T. Zhang, R. Takahashi, C. Fang, and S. Murakami, Phys. Rev. B **102**, 125148 (2020).

[32] Q.-B. Liu, Y. Qian, H.-H. Fu, and Z. Wang, npj Comput. Mater. **6**, 95 (2020).

[33] X. T. Wang, F. Zhou, Z. Y. Zhang, Z. M. Yu, and Y. G. Yao, Phys. Rev. B **106**, 214309 (2022).

[34] G. Liu, Z. Chen, P. Wu, and H. Xu, Phys. Rev. B **106**, 214308 (2022).

[35] R. Wang, B. W. Xia, Z. J. Chen, B. B. Zheng, Y. J. Zhao, and H. Xu, Phys. Rev. Lett. **124**, 105303 (2020).

[36] Y. J. Jin, Z. J. Chen, X. L. Xiao, and H. Xu, Phys. Rev. B **103**, 104101 (2021).

[37] Z. Huang, Z. Chen, B. Zheng, and H. Xu, npj Comput. Mater. **6**, 87 (2020).

[38] Y. Liu, X. Chen, and Y. Xu, Adv. Funct. Mater. **30**, 1904784 (2020).

[39] P. C. Sreeparvathy, C. Mondal, C. K. Barman, and A. Alam, Phys. Rev. B **106**, 085102 (2022).

[40] X. Chen, J. Liu, and J. Li, Innovation **2**, 100134 (2021).

[41] X. Wang, T. Yang, Z. Cheng, G. Surucu, J. Wang, F. Zhou, Z, Zhang, and G. Zhang, Appl. Phys. Rev. **9**, 041304 (2022).

[42] Y. Yang, C. Xie, Y. Cui, X. Wang, and W. Wu, Phys. Rev. B **107**, 054310 (2023).

[43] Y. Yang, J. Wang, Y. Liu, Y. Cui, G. Ding, and X. Wang, Phys. Rev. B **107**, 024304 (2023).

[44] M. Zhong, H. Liu, J. Wang, C. Xie, H. Yuan, Z. Zhang, G. Ding, X. Wang, and G. Zhang, Phys. Rev. B **107**, 205406 (2023).

[45] Y. Yang, F. Zhou, J. Wang, Y. Liu, Y. Cui, G. Ding, and X. Wang, Appl. Phys. Lett. **122**, 232202 (2023).

[46] G. Ding, J. Wang, H. Chen, X. Zhang, and X. Wang, J. Mater. Chem. C **10**, 6530 (2022).

[47] X. T. Wang, Z. X. Cheng, G. Zhang, H. K. Yuan, H. Chen, and X.-L. Wang, Phys. Rep. **888**, 1 (2020).

[48] H. Ishizuka and Y. Motome, Phys. Rev. Lett. **109**, 237207 (2012).

[49] X.-S. Li, C. Wang, M.-X. Deng, H.-J. Duan, P.-H. Fu, R.-Q. Wang, L. Sheng, and D. Y. Xing, Phys. Rev. Lett. **123**, 206601 (2019).

[50] S. Nie, T. Hashimoto, and F. B. Prinz, Phys. Rev. Lett. **128**, 176401 (2022).

[51] D. F. Liu, E. K. Liu, Q. N. Xu, J. L. Shen, Y. W. Li, D. Pei, A. J. Liang, P. Dudin, T. K. Kim, C. Cacho, Y. F. Xu, Y. Sun, L. X. Yang, Z. K. Liu, C. Felser, S. S. P. Parkin, and Y. L. Chen, npj Quantum Mater. **7**, 11 (2022).

[52] Y. Jiao, F. Ma, C. Zhang, J. Bell, S. Sanvito, and A. Du, Phys. Rev. Lett. **119**, 016403 (2017).

[53] R. Wang, J. Z. Zhao, Y. J. Jin, Y. P. Du, Y. X. Zhao, H. Xu, and S. Y. Tong, Phys. Rev. B **97**, 241111(R) (2018).

[54] M. M. Hosen, G. Dhakal, K. Dimitri, P. Maldonado, A. Aperis, F. Kabir, C. Sims, P. Riseborough, P. M. Oppeneer, D. Kaczorowski, T. Durakiewicz, and M. Neupane, Sci. Rep. **8**, 13283 (2018).

[55] J. Wang, Phys. Rev. B **96**, 081107(R) (2017).

[56] W. Meng, X. Zhang, Y. Liu, X. Dai, and G. Liu, Phys. Rev. B **104**, 195145 (2021).

[57] Y. J. Jin, R. Wang, Z. J. Chen, J. Z. Zhao, Y. J. Zhao, and H. Xu, Phys. Rev. B **96**, 201102(R) (2017).

[58] L. Jin, X. Zhang, Y. Liu, X. Dai, X. Shen, L. Wang, and G. Liu, Phys. Rev. B **102**, 125118 (2020).

[59] T. He, X. Zhang, Y. Liu, X. Dai, G. Liu, Z.-M. Yu, and Y. Yao, Phys. Rev. B **102**, 075133 (2020).

[60] T. Yang, L. Jin, Y. Liu, X. Zhang, and X. Wang, Phys. Rev. B **103**, 235140 (2021).

[61] H. P. Zhang, X. M. Zhang, Y. Liu, X. F. Dai, G. Chen, and G. D. Liu, Phys. Rev. B **102**, 195124 (2020).

[62] H. P. Zhang, X. M. Zhang, T. He, X. F. Dai, Y. Liu, G. D. Liu, L. Wang, and Y. Zhang, Phys. Rev. B **102**, 155116 (2020).

[63] N. C. Frey, M. K. Horton, J. M. Munro, S. M. Griffin, K. A. Persson, and V. B. Shenoy, Sci. Adv. **6**, eabd1076 (2020).

[64] R. W. Zhang, X. D. Zhou, Z. Y. Zhang, D. S. Ma, Z. M. Yu, W. X. Feng, and Y. G. Yao, Nano Lett. **21**, 8749 (2021).

[65] T. He, X. Zhang, Y. Liu, X. Dai, L. Wang, and G. Liu, Phys. Rev. B **104**, 045143 (2021).

[66] L. Jin, X. Zhang, Y. Liu, X. Dai, L. Wang, and G. Liu, Phys. Rev. B **102**, 195104 (2020).

[67] T. L. He, Y. Liu, L. Tian, X. M. Zhang, W. Z. Meng, X. F. Dai, and G. D. Liu, Phys. Rev. B **103**, 085135 (2021).

[68] L. Liu, C. Wang, S. Yi, D. K. Kim, C. H. Park, and J.-H. Cho, Phys. Rev. B **99**, 220401(R) (2019).

[69] R. Wang, Y. J. Jin, J. Z. Zhao, Z. J. Chen, Y. J. Zhao, and H. Xu, Phys. Rev. B **97**, 195157 (2018).

[70] T. He, X. Zhang, L. Wang, Y. Liu, X. Dai, L. Wang, and G. Liu, Phys. Rev. B **106**, 075155 (2022).

[71] H.-S. Jin, Y.-J. Song, W. E. Pickett, and K.-W. Lee, Phys. Rev. Mater. **3**, 021201(R) (2019).

[72] T. He, X. Zhang, T. Yang, Y. Liu, X. Dai, and G. Liu, Phys. Rev. Mater. **5**, 024205 (2021).

[73] J. Zou, Z. He, and G. Xu, npj Comput. Mater. **5**, 96 (2019).

[74] Y. Xu, L. Elcoro, Z.-D. Song, B. J. Wieder, M. Vergniory, N. Regnault, Y. Chen, C. Felser, and B. A. Bernevig, Nature (London) **586**, 702 (2020).

[75] X. Li and J. Yang, Natl. Sci. Rev. **3**, 365 (2016).

[76] M. C. Payne, M. P. Teter, D. C. Allan, T. A. Arias, and J. D. Joannopoulos, Rev. Mod. Phys. **64**, 1045 (1992).

[77] J. Hafner, J. Comput. Chem. **29**, 2044 (2008).

[78] J. P. Perdew, K. Burke, and M. Ernzerhof, Phys. Rev. Lett. **77**, 3865 (1996).

[79] A. A. Mostofi, J. R. Yates, Y.-S. Lee, I. Souza, D. Vanderbilt, and N. Marzari, Comput. Phys. Commun. **178**, 685 (2008).

[80] M. P. Lopez Sancho, J. M. Lopez Sancho, and J. Rubio, J. Phys. F: Met. Phys. **14**, 1205 (1984).

[81] M. P. Lopez Sancho, J. M. Lopez Sancho, and J. Rubio, J. Phys. F: Met. Phys. **15**, 851 (1985).

[82] X. Gonze and C. Lee, Phys. Rev. B **55**, 10355 (1997).

[83] M. Born and K. Huang, *Dynamical Theory of Crystal Lattices* (Clarendon, Oxford, 1954).

[84] M. E. Tuckerman, P. J. Ungar, T. Rosenvinge, and M. L. Klein, J. Phys. Chem. **100**, 12878 (1996).

[85] See Supplemental Material at http://link.aps.org/supplemental/10.1103/PhysRevB.108.054424 for an energy comparison of the FM, AFM, and NM states in the $2 \times 2 \times 1$ and $1 \times 1 \times 2$ supercells, the magnetic ground state and band structures calculated using the SCAN meta-GGA functional, the band structure calculated by Wannierization, orbital-resolved band structures contributed by Ni-d orbitals, and band structures under electron doping, etc.

[86] Z. Wang, A. Alexandradinata, R. J. Cava, and B. A. Bernevig, Nature (London) **532**, 189 (2016).

[87] J. Ma, C. Yi, B. Lv, Z. Wang, S. Nie, L. Wang, L. Kong, Y. Huang, P. Richard, P. Zhang, K. Yaji, K. Kuroda, S. Shin, H. Weng, B. A. Bernevig, Y. Shi, T. Qian, and H. Ding, Sci. Adv. **3**, e1602415 (2017).

[88] Z. F. Wang, B. Liu, and W. Zhu, Phys. Rev. Lett. **123**, 126403 (2019).

[89] M. Ezawa, Phys. Rev. B **94**, 155148 (2016).

[90] T. Zhang, Z. Cui, Z. Wang, H. Weng, and Z. Fang, Phys. Rev. B **101**, 115145 (2020).

[91] S.-S. Wang, Y. Liu, Z.-M. Yu, X.-L. Sheng, and S. A. Yang, Nat. Commun. **8**, 1844 (2017).

[92] H. B. Nielsen and M. Ninomiya, Nucl. Phys. B **185**, 20 (1981).

[93] H. B. Nielsen and M. Ninomiya, Nucl. Phys. B **193**, 173 (1981).

[94] J. Xiong, S. K. Kushwaha, T. Liang, J. W. Krizan, M. Hirschberger, W. Wang, R. Cava, and N. P. Ong, Science **350**, 413 (2015).

[95] Y. Gao, S. A. Yang, and Q. Niu, Phys. Rev. B **95**, 165135 (2017).

[96] P. J. W. Moll, N. L. Nair, T. Helm, A. C. Potter, I. Kimchi, A. Vishwanath, and J. G. Analytis, Nature (London) **535**, 266 (2016).

[97] S. Guan, Z.-M. Yu, Y. Liu, G.-B. Liu, L. Dong, Y. Lu, Y. Yao, and S. A. Yang, npj Quantum Mater. **2**, 23 (2017).

[98] X. Dai, H.-Z. Lu, S.-Q. Shen, and H. Yao, Phys. Rev. B **93**, 161110(R) (2016).

[99] B. Roy, P. Gaswami, and V. Juricic, Phys. Rev. B **95**, 201102(R) (2017).

[100] J. Sun, R. C. Remsing, Y. Zhang, Z. Sun, A. Ruzsinszky, H. Peng, Z. Yang, A. Paul, U. Waghmare, X. Wu, M. L. Klein, and J. P. Perdew, Nat. Chem. **8**, 831 (2016).

[101] J. Sun, A. Ruzsinszky, and J. P. Perdew, Phys. Rev. Lett. **115**, 036402 (2015).